Separation Science and Technology
Publication details, including instructions for authors and subscription information:
http://www.informaworld.com/smpp/title~content=t713708471

Modeling of Particle Separations in Complex Flows

P. Daskopoulos[a]; A. M. Lenhoff[a]
[a] Department of Chemical Engineering, University of Delaware, Newark, Delaware

To cite this Article Daskopoulos, P. and Lenhoff, A. M.(1991) 'Modeling of Particle Separations in Complex Flows', Separation Science and Technology, 26: 8, 1013 — 1050
To link to this Article: DOI: 10.1080/01496399108050512
URL: http://dx.doi.org/10.1080/01496399108050512

SEPARATION SCIENCE AND TECHNOLOGY, 26(8), pp. 1013–1050, 1991

Modeling of Particle Separations in Complex Flows

P. DASKOPOULOS and A. M. LENHOFF*
DEPARTMENT OF CHEMICAL ENGINEERING
UNIVERSITY OF DELAWARE
NEWARK, DELAWARE 19716

Abstract

Separations of micron-sized particles are generally dominated by body forces and hydrodynamic effects, which must be explicitly included in any mechanistic models of such separations. Accommodating complex flows is an especially challenging component of such modeling, and this paper illustrates an effort to do so for the special case of a particle fractionation process performed in a rotating coiled tube. The separation is based on the combined effects of rotation and axial flow; the body force is thus centrifugal, while the complex hydrodynamics arise from the secondary flows that occur in addition to the axial convection in rotating curved tubes. The model is assembled in three stages. First, single-particle motion in a rotating tube is considered, and the effects of various parameters are elucidated. Next, these results are used in modeling the behavior of monodisperse sets of particles in order to account for a distribution of possible initial conditions. Finally, these results are used with a Gaussian quadrature scheme to simulate the behavior of a polydisperse particle population. A comparison with experimental results is presented for the steady-state and dynamic aspects of particle fractionation; agreement is good for the former, but discrepancies remain for the latter, possibly because of uncertainties in the particle size distributions.

INTRODUCTION

Particle separations are important in a large number of applications in such fields as biotechnology, mineral processing, and materials science. For particles on the order of microns in size, Brownian transport is too weak to be of practical use, and it is generally necessary to employ body forces in some way, e.g., centrifugation, electrostatic or magnetic separations, etc. Whatever the basis for the separation, most processes are implemented with the particles in a suspending fluid, leading to a need to account for hydrodynamic effects as well as the body force giving rise to

*To whom correspondence should be addressed.

the separation. The hydrodynamics in many separations processes are relatively simple—in sedimentation field flow fractionation (SFFF) (*1*), for example, the flow is laminar and rectilinear—and these conditions often reduce the difficulty of obtaining a quantitative theoretical understanding and make these processes easier to design. It is, however, possible to increase the number of degrees of freedom in designing particle separations when more complex hydrodynamics are considered and even exploited. Such approaches may be desirable, especially for difficult separations, when staged or cyclic operation is usually needed. The disadvantage of this is, however, the complexity of the physical situation and thus of trying to develop quantitative models for design purposes.

This paper deals with such a hydrodynamically complex process, namely the fractionation of particles by manipulating the axially imposed flow in a rotating helical coil (*2*). The interaction of centrifugal and hydrodynamic effects (including secondary flows) leads to fractionation based on differences in particle size and density, with proof-of-principle experiments having been performed on a slurry of ferric oxide and zirconium oxide particles. The object of the work reported here is to develop a mechanistic model of the process that can be used to examine the effects of design and operating parameters on process performance. More important, however, is the broader motivation of examining the feasibility of modeling particle separations in which complex hydrodynamics are present. As the results presented below demonstrate, agreement between model predictions and experimental data is very good in some respects and less so in others, and possible reasons for these observations are discussed.

The process of interest developed from an earlier periodic concentration technique in a spinning helical coil, originally suggested by Adler and coworkers (*3–5*), who also presented a relatively simple first-order model (*5*) as well as a more detailed model of a related but simpler fractionation process (*6*). The basic idea of this approach was to couple a periodic local separation, alternating between depletion and enrichment of a component in a liquid–solid mixture, with an externally induced back-and-forth axial fluid motion, in order to achieve separation. This method thus combines the cyclic nature of parametric pumping (*7, 8*) with the physical mechanisms employed in SFFF (*9–11*). Adler et al. (*4*) have, however, noted two important differences from SFFF. First, secondary flows are used to enhance the separation, and second, the cyclic method can be used for concentrating and/or separating mixtures, while SFFF always leads to dilution.

The process variant examined in this paper accomplishes batch fractionation of fine particle dispersions according to size and/or density by cyclic repetition of a five-step sequence as sketched in Fig. 1 (*2*). The coil is connected to two well-stirred reservoirs through a spinning seal assembly,

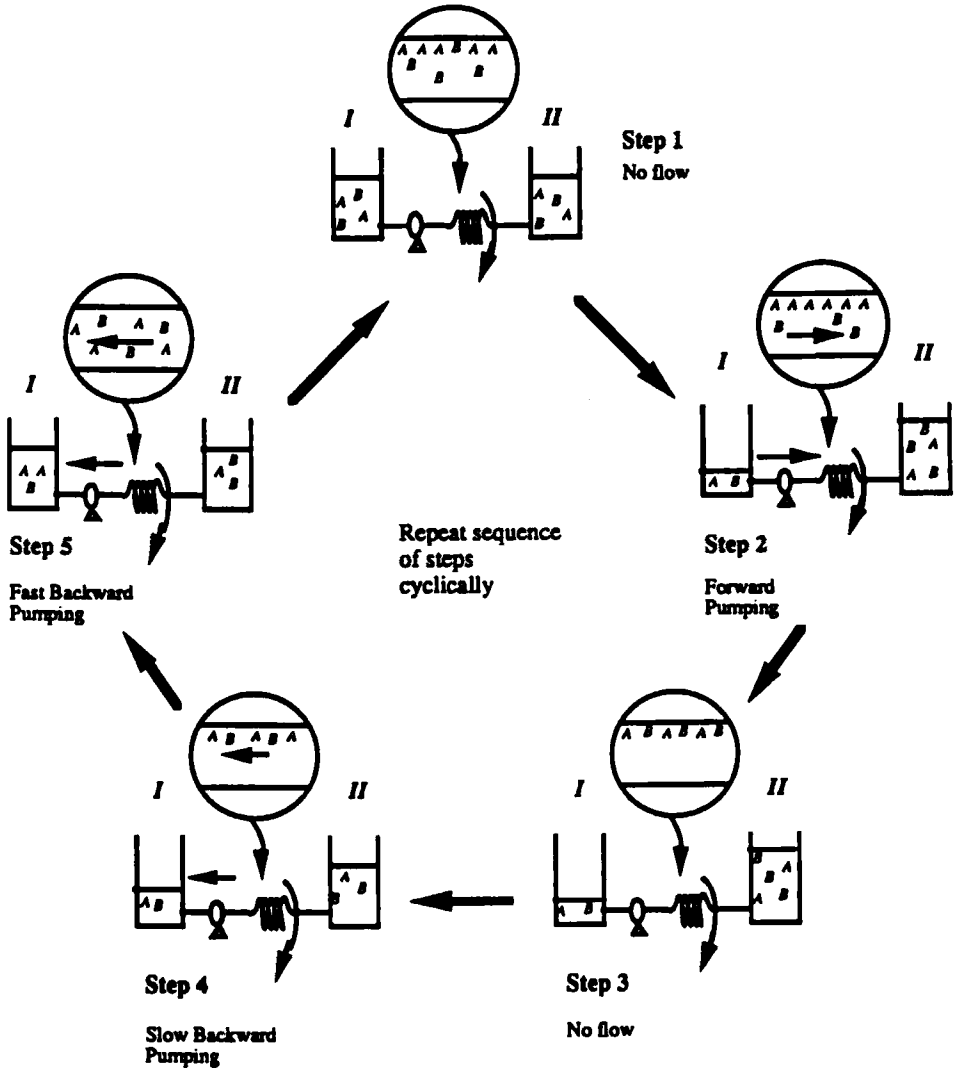

FIG. 1. Schematic diagram of cyclic batch separation sequence (after Ref. 2).

with a bidirectional pump used to move fluid through the coil, which rotates continuously throughout the process. Initially the concentrations of particles A and B are uniform throughout the entire system, and the objective is to fractionate the mixture based on A's having a larger sedimentation velocity than B. During the first step there is no axial flow through the coil and the particles in the coil sediment under the influence of the external

field. The time of this step is chosen to be long enough that A sediments completely, but short enough that a substantial amount of B remains in suspension. In the second step, fluid is pumped from reservoir I through the coil toward reservoir II at a rate low enough that the secondary flows induced are not strong enough to resuspend particles of A. During this step only particles of species B are therefore moved toward reservoir II. A complete sedimentation step (third step) follows, during which all the suspended particles (mainly B) drop out. The fourth step is displacement of fluid toward reservoir I sufficiently slowly not to disturb the sedimented particles in the coil. Finally, during the fifth step, a rapid displacement toward reservoir I induces strong secondary flows that resuspend the particles of both species A and B, which are then carried toward reservoir I by the axial flow. Cyclic repetition of the steps leads to the net movement of A toward reservoir I and of B toward II and thus provides the basis for fractionation.

The key to separation is particle movement in opposite directions during forward and backward pumping: whether a particle eventually ends up in reservoir I or II depends on the difference between the distances traveled during the opposite pumping steps. Hence there exists a cut-off radius, marked a_c on the distribution in Fig. 2, below which particles display net migration toward reservoir II and above which they display net migration toward reservoir I. The value of a_c depends on particle characteristics and operating conditions. The net migration toward either reservoir is amplified by the cyclic repetition of the steps, with most particles ending up in one reservoir or the other. However, a particle fraction with radii close to a_c is characterized by similar extents of forward and backward axial migration during the cycle, and thus displays little net motion toward either end of the coil. This results in a fraction of particles in the radius range Δa, shown in Fig. 2, that will not be able to leave the coil in the preassigned number of cycles.

Differences in behavior among particles in the distribution also become apparent in step 3, the complete sedimentation step. If this step is too short, a critical particle radius exists, a_b in Fig. 2, below which the particles are still in suspension after the end of step 3, resulting in migration in the opposite direction during the slow backward pumping step. Since fractionation is based on transporting the small-particle sample toward reservoir II, backward motion during this step is undesirable and can result in decreased efficiency.

The overall behavior of the polydisperse system under consideration is determined by the position of a_c relative to the region of the size distribution that contains the largest fraction of sample mass. The cut-off size a_c can be manipulated by varying the process parameters, and one objective of

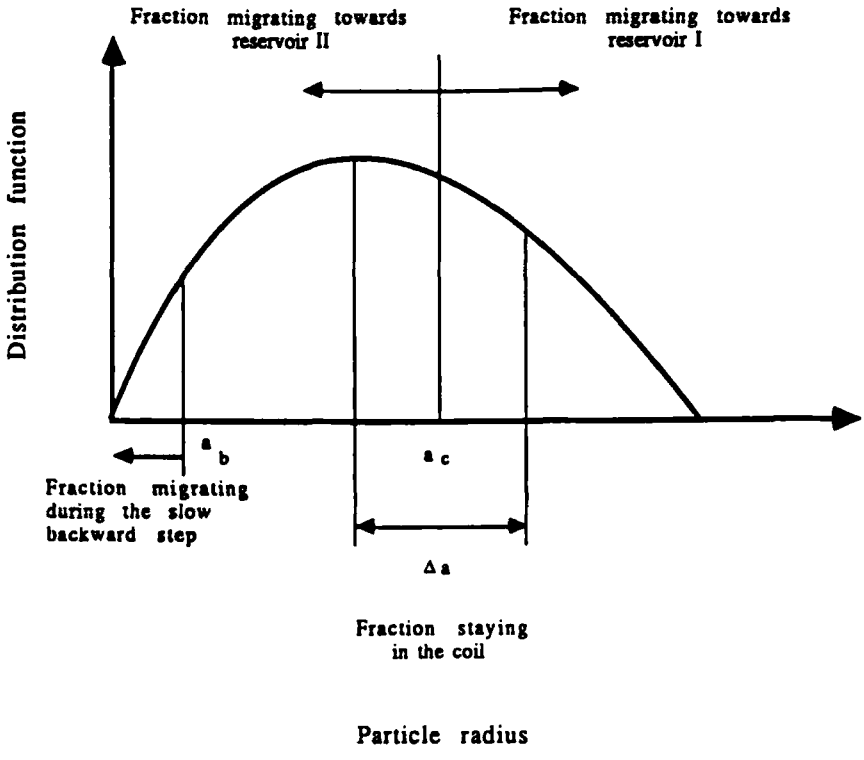

FIG. 2. Distribution of particle behavior as a function of size.

developing a predictive model is to relate a_c to the various parameters. However, this provides information only on the final steady-state after an infinite number of cycles. It is also important to be able to model the dynamic response of the system, i.e., the approach to the steady state as a function of time; this is more complicated and depends strongly on the actual particle size distribution. The work presented here addresses both aspects.

Lennartz et al. (*2*) demonstrated the performance of the particle fractionation scheme by separating particles of ferric oxide and zirconium oxide in a radius range between approximately 1 and 15 μm. Key process design and operating parameters are presented in Tables 1–3, and they form the basis for our model calculations to be compared with Lennartz et al.'s experimental data.

A mechanistic model suitable for predictive exploration of a large region of the parameter space requires detailed modeling of several aspects: single-

TABLE 1
Experimental Particle Systems (2)

Properties	Ferric oxide, Fe_2O_3	Zirconium oxide, ZrO_2
Density, kg/m³	5.15×10^3	5.75×10^3
Initial concentration, kg/m³	3	3.2
Shape	Nearly spherical	Nearly spherical
Particle radius, μm:		
50 wt%	1.5–2	1–7.5
80 wt%	0.5–2.5	0.25–10
95 wt%	0.25–5	0.15–12.5
100 wt%	<10	<15

TABLE 2
System Structure (2)

Initial reservoir volumes	290 mL each
Connecting line volumes	6 mL each
Coil volume	54 mL
Seal assembly volume	9 mL
Coil	5½ turns PTFE tubing Tube radius 2.2 mm Coil radius 10.2 cm

TABLE 3
Experimental Procedure (2)

Coil rotation rate	160 rpm, Ta = 1560
Cycle sequence:	
Step 1	No axial flow Duration: 2.5 s
Step 2	Forward pumping, Re = 318, D = 578 Duration: 18.18 s
Step 3	No axial flow Duration: 90 s
Step 4	Slow backward pumping, Re = 318, D = 586 Duration: 4.55 s
Step 5	Fast backward pumping, Re = 16192, D > 10,000 Duration: 0.27 s

phase flow in a rotating helical coil, motion of a single particle in a flow and gravitational field, and treatment of polydisperse particle populations. We have studied the hydrodynamic problem in detail (*12*), including the existence of multiple solutions; in this paper only the primary steady-state solution is used. The remainder of the model features are described in the next section, and results and conclusions are presented separately.

MODEL DESCRIPTION

Single-Particle Motion

Stokes' law provides the simplest description of particle motion through a fluid, but it applies only to the steady motion, at velocity $\mathbf{U}_p$, of a rigid spherical particle of radius a_p through an unbounded quiescent fluid of viscosity μ. Many additional complications can be accounted for, as summarized most extensively by Happel and Brenner (*13*), but also elsewhere (*14–16*). Additional effects include fluid motion, particle shape, presence of walls, inertial effects, and interparticle interactions, and these may be accounted for to varying degrees of accuracy. Generalization of Stokes' law using the method of reflections yields the approximate result (*13*)

$$\begin{aligned}\mathbf{F} &= -6\pi\mu c\left(\boldsymbol{\Phi}_\infty^{-1} - \frac{c}{l}\mathbf{k}\right)^{-1}\cdot(\mathbf{U}_p - [\mathbf{v}_\infty]_0) \\ &\equiv -6\pi\mu c\boldsymbol{\Phi}\cdot(\mathbf{U}_p - [\mathbf{v}_\infty]_0)\end{aligned} \tag{1}$$

for the hydrodynamic force on a rigid particle of arbitrary shape moving at velocity $\mathbf{U}_p$ near a wall in a fluid that would be moving at velocity $\mathbf{v}_\infty$ if undisturbed by the particle. c is a characteristic particle dimension, l is a characteristic distance of the system, and the subscript 0 implies evaluation at the location of the sphere center. $\boldsymbol{\Phi}_\infty$ is a dimensionless, symmetric dyadic, the Stokes resistance tensor, applying to motion of the particle in an unbounded fluid. It is an intrinsic and invariant property of the particle, dependent solely on the shape of the particle and independent of the size, velocity, and orientation of the particle and of the properties of the fluid through which it moves. $\mathbf{k}$ is a wall-effect tensor, an intrinsic property of the shape of the bounding walls and of the location of the center of the particle relative to the boundaries, and is independent of such factors as the shape, size, orientation, and velocity of the particle, the properties of the fluid, and the size of boundaries. Happel and Brenner (*13*) provide a compilation of the calculated values of the components of the wall-effect tensor for various simple boundaries. Because of the nature of $\boldsymbol{\Phi}_\infty$ and $\mathbf{k}$, $\boldsymbol{\Phi}$ is also a dimensionless symmetric dyadic independent of the fluid prop-

erties and of the magnitude and direction of $\mathbf{U}_p$. However, it depends on the sizes and shapes of particle and wall, the location of the center of the particle relative to the wall, and its orientation.

Equation (1) forms the basis of the model used here. In the absence of any detailed particle shape information for the materials used by Lennartz et al. (*2*), particles were assumed to be spherical, in which case $\mathbf{\Phi}_\infty$ is a unit tensor. The treatment of wall effects is a first-order one, and requires modification for instance when the particle is very close to the wall: lubrication theory is then more suitable than the method of reflections (e.g., Ref. *17*). However, since typical particle sizes used experimentally were so much smaller than the tube cross-section, the overall wall effect on particle motion is small enough that Eq. (1) was used throughout.

The situation of most interest is that where inertial forces are small compared to viscous forces, i.e., the Stokes regime. Omitting the terms describing inertial effects from the underlying equations of motion leads to a linear system, at least for Newtonian fluids, and this significantly simplifies the mathematical analysis of the system. Because of the small particle sizes considered here and the resulting small particle Reynolds numbers, the assumption of negligible inertial forces is retained. The effects of inertia on particle motion have been examined mostly for rigid spherical particles and for simple flows (*15*), and understanding is far from comprehensive. What is clear, however, is that for spherical particles, incorporation of inertial effects can result in a wider range of phenomena than for the Stokes limit, including lateral migration, orbital drift, and rotational effects in sedimentation. In the context of this work, the most important inertial effect is the additional lift force acting on the particle, which gives rise to lateral translational motion. This lift force has been calculated for both unbounded (*18*, *19*) and bounded (*20–22*) domains, but only for idealized flow fields. A rough estimate of the lift force arising because of weak inertial effects can be obtained by using the analysis of Ho and Leal (*20*) for two-dimensional unidirectional flows; for conditions typical of the fractionation experiments, this force is $\sim 4 \times 10^{-3}$ and 1×10^{-6} the drag force for particles with a radius of 15 and 1 μm, respectively (*23*). Inertial effects can thus be neglected relative to viscous forces.

Techniques for accounting for hydrodynamic interactions between particles are summarized by Happel and Brenner (*13*). Describing such interactions requires accounting for particle shapes and sizes, their relative orientations, and the distance between them, their orientation individually relative to possible externally imposed fields, and the motion of the fluid in which they are immersed. In general, analytic solutions are not possible, and perturbation methods are usually used. Incorporating these into the kind of model of interest here was not feasible, and interparticle interac-

tions were thus neglected; this is true not just for hydrodynamic but also for colloidal interactions. This neglect is a serious omission only when the local particle concentration is quite high, and this occurs in the particle fractionation scheme only near the wall when the particles are sedimented. This issue is discussed further later in the paper.

The descriptions summarized above can be combined with body forces to obtain the hydrodynamic force on a particle immersed in the fluid flowing through a rotating coiled tube. For a tube of small curvature, a rotating toroidal coordinate system (r,α',θ) can be used (Fig. 3), and the force on the particle is then given, in tensorial form, by Eq. (1), corrected for the fictitious body forces introduced by the rotating coordinate system:

$$\mathbf{F} = -6\pi\mu a_p\left(\mathbf{\Phi}_\infty^{-1} - \frac{a_p}{l}\mathbf{k}\right)^{-1}\cdot(\mathbf{U}_p - [\mathbf{v}_\infty]_0) - \frac{4}{3}\pi a_p^3(\rho_p - \rho)[\mathbf{\Omega}\times(\mathbf{\Omega}\times\mathbf{r}) + 2\mathbf{\Omega}\times\mathbf{U}_p] \quad (2)$$

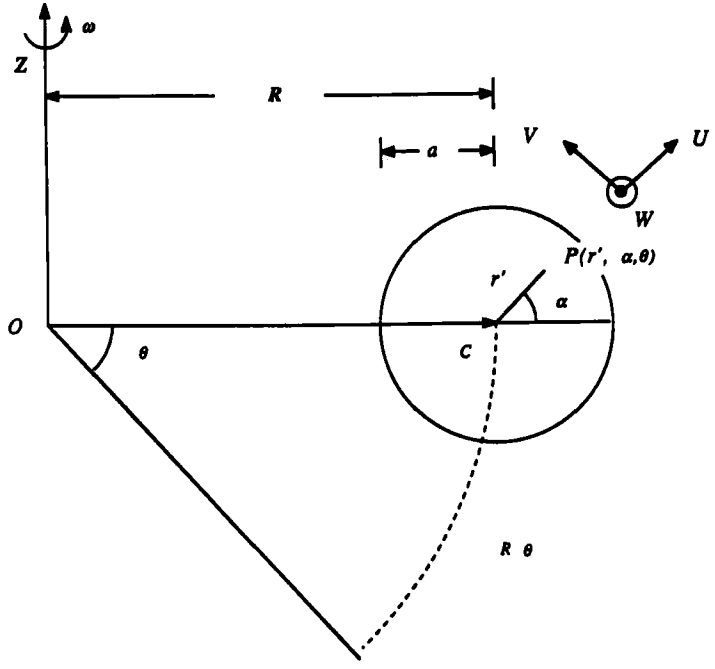

FIG. 3. Rotating toroidal coordinate system.

Here ρ and ρ_p are the fluid and the particle density, respectively, $\mathbf{\Omega}$ is the angular velocity, $\mathbf{r}$ is the particle position vector, $[\mathbf{v}_\infty]_0$ is the undisturbed fluid velocity (in the absence of a particle), and the characteristic distance l appearing in Eq. (1) is defined as the distance of the particle center from the wall.

The Stokes resistance tensor $\mathbf{\Phi}_\infty$ is a unit tensor for the spherical shape assumed, while for the wall-effect tensor the motion of the particle can be decomposed into motions perpendicular to a rigid plane wall (r' direction) and parallel to it (α and θ directions). The system is approximated by a plane wall tangent to the cylindrical surface, with curvature ignored. Falade and Brenner (*24*) showed that the planar approximation is the zeroth-order term in a regular perturbation scheme, valid when the characteristic distance of the particle from the wall is much smaller than the wall curvature radius but still much larger than the size of the particle. The wall-effect tensor, $\mathbf{k}$, can then be written as

$$\mathbf{k} = \begin{pmatrix} 9/8 & 0 & 0 \\ 0 & 9/16 & 0 \\ 0 & 0 & 9/16 \end{pmatrix} \tag{3}$$

For a particle moving perpendicularly toward or away from the wall, wall effects are significant up to a distance of a few particle radii from the wall, (e.g., leading to an increase in the Stokes resistance of 230, 13, 6, and 1% for distances of 1, 10, 20, and 100 particle radii, respectively), with an infinite drag on the particle predicted at a distance 0.125 particle radii. Thus the wall effects can be thought of as playing the role of a steep potential acting close to the wall, tending to prevent the particle from coming in contact with it. Due to the small particle sizes considered in this work, wall effects are significant in only a small part of the computational domain. Lubrication and curvature effects are ignored since they play a role only when the particle is very close to the walls and are negligible when the particle is more than a particle radius from the wall.

Particle trajectories are calculated by using Eq. (2) in conjunction with Newton's second law. In a toroidal coordinate system rotating at angular velocity ω, with the axial distance defined as $s' = R\theta$ (R is the coil radius), this results in a system of six first-order differential equations for the position and velocity components of the particle:

$$\partial s'/\partial t = W_p \tag{4}$$

$$\partial r'/\partial t = U_p \tag{5}$$

$$r' \frac{\partial \alpha}{\partial t} = V_p \tag{6}$$

$$\frac{4}{3}\pi a_p^3 \rho_p \frac{\partial W_p}{\partial t} = -6\pi\mu a_p \left(1 - \frac{9}{16}\frac{a_p}{a - r'}\right)^{-1} (W_p - W)$$

$$- \frac{8}{3}\pi a_p^3 (\rho_p - \rho)\omega(U_p \cos\alpha - V_p \sin\alpha) \tag{7}$$

$$\frac{4}{3}\pi a_p^3 \rho_p \frac{\partial U_p}{\partial t} = -6\pi\mu a_p \left(1 - \frac{9}{8}\frac{a_p}{a - r'}\right)^{-1} (U_p - U)$$

$$+ \frac{8}{3}\pi a_p^3 (\rho_p - \rho)\omega^2 R \cos\alpha + \frac{4}{3}\pi a_p^3 (\rho_p - \rho)\omega W_p \cos\alpha \tag{8}$$

$$\frac{4}{3}\pi a_p^3 \rho_p \frac{\partial V_p}{\partial t} = -6\pi\mu a_p \left(1 - \frac{9}{16}\frac{a_p}{a - r'}\right)^{-1} (V_p - V)$$

$$- \frac{8}{3}\pi a_p^3 (\rho_p - \rho)\omega^2 R \sin\alpha - \frac{4}{3}\pi a_p^3 (\rho_p - \rho)\omega W_p \sin\alpha \tag{9}$$

Here ω is the angular velocity of the coil.

Dimensionless quantities are introduced by scaling planar velocities by a sedimentation velocity in the centrifugal field and axial velocities by the rotational velocity. A characteristic time is derived from the mobility of the particle, and lateral and axial lengths are scaled relative to the tube and coil radii, respectively:

$$U_p = \frac{2}{9}\frac{a_p^2 \Delta\rho R\omega^2}{\mu} u_p, \qquad V_p = \frac{2}{9}\frac{a_p^2 \Delta\rho R\omega^2}{\mu} v_p,$$

$$W_p = \omega R w_p, \qquad t = \frac{2}{9}\frac{\rho_p a_p^2}{\mu}\tau, \qquad r' = ar, \qquad s' = Rs \tag{10}$$

Here $\Delta\rho = \rho_p - \rho$. The fluid velocities (U,V,W) are scaled as in the corresponding single-phase hydrodynamic problem (*12*):

$$u = aU/\nu, \qquad v = aV/\nu, \qquad w = \frac{aW}{\nu}\sqrt{\frac{2a}{R}}$$

with $\nu = \mu/\rho$ the kinematic viscosity. Equations (4) to (9) can then be written in dimensionless form as

$$\frac{\partial s}{\partial \tau} = \frac{1}{9}\sigma\epsilon \mathrm{Ta}^2\sqrt{\frac{\delta}{2}}\, w_p \tag{11}$$

$$\frac{\partial r}{\partial \tau} = \frac{1}{162}\sigma(\sigma - 1)\epsilon^4 \mathrm{Ta}^2 u_p \tag{12}$$

$$\frac{\partial \alpha}{\partial \tau} = \frac{1}{162}\sigma(\sigma - 1)\epsilon^4 \mathrm{Ta}^2 \frac{v_p}{r} \tag{13}$$

$$\frac{\partial w_p}{\partial \tau} = -\left(\frac{16(1-r)}{16(1-r) - 9\epsilon}\right) w_p + \frac{2}{\mathrm{Ta}}\left(\frac{16(1-r)}{16(1-r) - 9\epsilon}\right) w - \frac{1}{81}(\sigma - 1)^2\epsilon^4\delta \mathrm{Ta}^2(u_p \cos\alpha - v_p \sin\alpha) \tag{14}$$

$$\frac{\partial u_p}{\partial \tau} = -\left(\frac{8(1-r)}{8(1-r) - 9\epsilon}\right) u_p + \frac{36}{\sigma - 1}\frac{1}{\epsilon^2 \mathrm{Ta}^2}\left(\frac{8(1-r)}{8(1-r) - 9\epsilon}\right) u + \cos\alpha + 2w_p \cos\alpha \tag{15}$$

$$\frac{\partial v_p}{\partial \tau} = -\left(\frac{16(1-r)}{16(1-r) - 9\epsilon}\right) v_p + \frac{36}{\sigma - 1}\frac{1}{\epsilon^2 \mathrm{Ta}^2}\left(\frac{16(1-r)}{16(1-r) - 9\epsilon}\right) v - \sin\alpha - 2w_p \sin\alpha \tag{16}$$

where the dimensionless parameters

$$\mathrm{Ta} = 2\sqrt{2\delta}\,\frac{a\omega R}{\nu}, \qquad \delta = a/R, \qquad \epsilon = a_p/a, \qquad \sigma = \rho_p/\rho \tag{17}$$

have been introduced. The Taylor number, Ta, is one of the two key hydrodynamic parameters in a rotating curved tube, the other being the Dean number $\mathrm{D} = Ga^3\sqrt{2\delta}/\mu\nu$, where G is the imposed axial pressure gradient. Since D affects the velocity components (u,v,w), it is a parameter

appearing indirectly in Eqs. (11) to (16). The curvature, δ, also affects the flow directly. ϵ and σ characterize the particle. The system of Eqs. (11) to (16) can be solved for any time τ for given initial particle position and velocity components and subject to the values of the five dimensionless parameters. Since the velocity field for viscous flow in curved spinning coils is known (*12*), the trajectory of a particle can be calculated by time integration of the system equations. The solution to the hydrodynamic problem applies to steady, fully-developed flow, so long enough process times relative to the characteristic viscous time are required for the decay of transients to allow applicability of the hydrodynamic results to the fractionation scheme. In this case the system equations become ordinary differential equations with respect to the time variable, and a variable-order implicit multistep method with an analytical Jacobian is used for their solution. In the numerical implementation, commercially available ordinary differential equation solvers (IMSL) were utilized.

Once an initial condition for a particle had been prescribed, integration in time was performed for the total time corresponding to the duration of the first step of the fractionation scheme (as shown in Table 3). The transition from one step of the cycle to the next was accomplished by modifying the velocity field describing the hydrodynamic problem, followed by integration in time to the end of the step. The final particle position during the previous step served as the initial condition for the subsequent one.

These procedures were not applied to the last step of the cycle, i.e., the fast backward pumping, which plays the role of a resuspension step and where turbulent flow conditions were used experimentally. This step was accounted for in the model by assuming all particles to be resuspended instantaneously and subsequently transported axially at the average flow velocity. For the assumption of complete, instantaneous resuspension to be valid, the flow conditions must be strong enough to ensure resuspension, and the duration of the step must be much greater than the time required for the particle to pass from the viscous layer near the wall to the turbulent core.

Both these requirements appear to be satisfied. First, the resuspension velocity for the particles can be calculated using any of a number of correlations; Zenz and Othmer's (*25*),

$$u^2 = 8ga_p\Delta\rho/(3\rho) \tag{18}$$

gives the fluid velocity, u, capable of resuspending a particle of radius a_p, with the acceleration g calculated from the rotation of the system. These u values can be compared to those at the particle centers, estimated from the velocity field in the viscous sublayer found from the standard theory

of turbulence (*26*). For the flow conditions and the geometry of interest, the thickness of the viscous sublayer is about 60 μm and the velocity gradient is about 63,600 s^{-1}. The result is a predicted safety margin of about 3 for 0.5 μm radius particles and about 10 for 10 μm ones, indicating that particles are indeed resuspended.

The assumption of instantaneous resuspension was tested by estimating the time required for the resuspension from a force balance on the particle, the contributions being the lift force and the centrifugal force. As mentioned previously, lift is due to inertial effects, and it appears to be unimportant in the fractionation scheme when flow is laminar. However, in the turbulent resuspension step the high shear rate in the viscous layer enhances lift, hence its inclusion here. The lift force can be estimated in any of a number of ways (*19*, as extended by Ref. *27*; *20*, *22*), and integration of the force balance then provides the trajectory of the particle perpendicular to the wall and an estimate of the time required for the particle to move from the viscous sublayer to the turbulent core of the fluid. These calculations (*23*) indicate that times on the order of 10^{-4} s are required, compared to the overall step duration of 0.27 s used in the experiments, so the assumption seems quite safe.

A complete analysis of resuspension should account for phenomena such as particle–particle interactions and the existence of multiple layers of particles at the wall, in view of the high effective concentrations that result. That the sedimented particles are not isolated individual particles presents a complication, but one that is difficult to accommodate accurately. However, since large particles are more easily resuspended (Eq. 18 and associated velocity estimate from shear rate), the turbulent flow is likely to be capable of resuspending a particle aggregate. The margin of safety in the assumption of instantaneous resuspension is large enough that it should not be affected by the presence of aggregates.

Multiparticle Systems

The modeling procedures described above are suitable for calculating the trajectories of single particles, and they must be modified to accommodate the particle populations used experimentally. Two factors must be accounted for. First, in a monodisperse multiparticle system there is a distribution of initial conditions over which averaging must be performed in order to characterize the behavior of the population. Second, polydispersity must be accounted for by averaging over the size distribution of the population. These issues are discussed separately below.

The initial condition is a very important parameter affecting the calculated axial migration of particles in the tube. Both the position and the

velocity of each particle are unknown at the start of a given cycle. The initial velocity does not affect the final results appreciably, since the first step is long enough for the effects of this velocity to be damped out. In all the simulations the initial velocities of the particles have thus been taken to be zero, and the validity of this assumption has been confirmed by control calculations using different initial velocities. The randomness in initial positions must, however, be accounted for. This was done by performing simulations for samples of particles with the same characteristics (i.e., size and density) initially distributed uniformly over the tube cross-section. Averaging over the sample provided the average properties, in this case axial motion of the population during the different steps of the fractionation technique. Different sample sizes were used until the desired accuracy was obtained, with consecutive samples required to differ by no more than 5% in this study. Larger sample sizes were not warranted in view of the uncertainties in the experimental data (*2*) with which comparison was made.

In order to incorporate the effects of the particle size distribution, a continuous distribution was used to describe the experimental systems. Continuous distributions have been used previously for the characterization of polydisperse systems (see, e.g., references in Ref. *28*), and similar techniques can be used for polydisperse particle systems, in this case to obtain a measure of the average extent of axial motion in the coil during a cycle of the separation scheme.

In principle, quantitative modeling of the process requires evaluation of the motion of all the particles in a continuous distribution and subsequent averaging over the actual distribution function. For example, if ℓ is the extent of axial migration of particles of radius a_p, and $g(a_p)$ is the normalized density distribution function between a minimum (a_{min}) and a maximum (a_{max}), the average axial migration of the sample is given as

$$\bar{\ell} = \int_{a_{min}}^{a_{max}} \ell(a_p) g(a_p) \mathrm{d}a_p \tag{19}$$

In practice, the integral is evaluated by summation over a set of discrete points, a_i,

$$\bar{\ell} = \sum_{i=1}^{n} \ell(a_i) W_i \tag{20}$$

where W_i are weights in the quadrature. Optimal quadrature efficiency is obtained by using Gaussian quadrature points, giving rise to different points

and weighting functions, depending on the continuous distribution used (*29*). A similar approach has been used for phase equilibrium calculations for hydrocarbon mixtures (*30*).

Three asymmetric distributions were used in this work to model the experimental systems, namely the beta, Pearson III, and log-normal types (see, e.g., Ref. *31*). Since the last two of these exist over an infinite range, while the experimental population has a finite upper size limit, they were renormalized over the range of interest. The experimental measurements of Table 1 were used to fit normalized continuous distributions characterizing the zirconium and ferric oxide samples. The two parameters for each theoretical distribution were usually obtained by requiring the 50 and 80 wt% fractions of the population to be distributed as a function of particle size in the range suggested by the experimental data. Alternative approaches can also be used, e.g., fitting total mass up to particle radii of 7.5 and 10 μm, or a least-squares fit to the 50, 80, and 95% cutoff sizes; different parameters would then be obtained. Most of the results reported below were based by fitting the 50 and 80% fractions to a beta distribution

$$g(x) = \frac{x^{a-1}(1 - x)^{b-1}}{B(a,b)} \tag{21}$$

where B is the beta function, but the sensitivity of the results to the distribution used is discussed later.

For each particle size included as a Gaussian quadrature point, the 100 cycles of the process were simulated as follows. Initially the concentrations of A and B throughout the system were assumed to be uniform. The two reservoirs were considered as being well mixed at all times, while uniform migration, at the mean velocity (averaged over initial positions in the cross-section), was assumed in the coil. Inclusion of dispersion would be both difficult and unwarranted by the nature of the experimental data. During the first cycle, concentration discontinuities develop between the reservoirs and the adjacent ends of the coil, and the uniform migration assumed in the coil then results in propagation of the fronts through the coil, with new fronts created during every cycle. These fronts move through the coil at different rates, which depend on the particle size. The concentrations in the reservoirs change because of particle transport into and out of the coil during each cycle. The displacements of the concentration fronts in the coil were monitored during the various steps of the cycle for a sequence of 100 cycles. In order to account for sampling of the reservoirs in the experiments, their volume was readjusted every 25 cycles. Simulations were performed for multiple particle populations, each of uniform size. Quad-

rature over the particle size then provided concentrations (by weight) of the two different types of particles as a function of cycle number.

Knowledge of the cut-off particle size (a_c in Fig. 2) is adequate for characterizing the ultimate fractionation accomplished, but an accurate description of the tails is essential for predicting the dynamics of the fractionation. Since the quadrature scheme places few points in the tail, convergence was improved by incorporating the additional information provided by the cut-off size in the simulations. For this purpose the quadrature procedure was modified by incorporation of additional points to take into account the cut-off size and the resulting splitting of the sample into two fractions exhibiting qualitatively different migration behavior, namely net migration in opposite directions. Similar action was taken to account for the fraction expected to remain in the coil for more than 100 cycles (Δa in Fig. 2). The additional points were placed in the middle of the respective size ranges.

RESULTS AND DISCUSSION

Single-Particle Motion

The kinds of particle separations of interest here exploit differences in axial migration of individual particles arising from differences in particle characteristics. These differences in axial migration result from differences in trajectories in the tube cross-section, so both lateral and axial motion must be examined. The major process parameters apart from particle characteristics (size and density) are hydrodynamic (relative strength and/or direction of axial flow and rotation of the system), but the effects of different initial conditions are also significant. Because of the importance of several parameters and the strong interactions among them, a comprehensive exploration of the parameter space is not performed; instead, the particle fractionation scheme discussed earlier is used as the basis for the discussion, with qualitative arguments and estimates presented first and more detailed computational results shown subsequently. The emphasis is on the first two steps in the fractionation process, where differential behavior is most clearly apparent.

The first step in the fractionation scheme is an incomplete sedimentation step exploiting differences in settling rates arising from different particle characteristics. A Stokes sedimentation velocity,

$$U_s = \frac{2a_p^2 \Delta\rho\omega^2 R}{9\mu} \tag{22}$$

can be used, with the centrifugal acceleration assumed constant throughout the tube because of the small curvature of the system. Knowledge of U_s allows the duration of the sedimentation step to be chosen so as to ensure the sedimentation of heavier and/or larger particles while lighter and/or smaller ones remain in suspension. High rotational speeds accelerate the sedimentation process but also decrease the sensitivity of the method for separating two particles of different size and/or density, while low rotation rates improve resolution at the cost of larger cycle times; these considerations affect the choice of a suitable rotational velocity for the coil.

The second step of the fractionation scheme is more complex in that it involves axial migration. Fluid is pumped through the coil, carrying with it the particles that have not sedimented in the previous centrifugation step. The effects of rotation now interact with those of axial flow and influence the trajectory of a particle in the cross-sectional plane of the tube. This trajectory is a function of the initial position of the particle, its physical characteristics, and the nature of the flows. Two limiting situations are possible. The first is when the secondary flows are strong enough to keep the particle in suspension, resulting in axial migration along a spiral path due to the axial flow. The second situation is when the particle sediments to the tube wall despite the secondary flows, resulting in very slow axial migration because of the low axial velocities near the wall. An additional concern beyond the fate encountered by a suspended particle is that particles that sedimented in the first step should not be resuspended.

Which of the two limiting situations is seen for a given particle requires consideration of the relative strength of centrifugal forces and secondary flows, and thus depends on both particle and operating parameters. Equation (22) provides a measure of the sedimentation velocity, while the secondary flow velocities are obtained from hydrodynamic calculations. The ratio of the characteristic secondary flow velocity to the sedimentation velocity can then be written as

$$U/U_s = 36u/\{\epsilon^2(\sigma - 1)\mathrm{Ta}^2\} \tag{23}$$

where u is a dimensionless secondary flow velocity. The right-hand side of Eq. (23) is essentially the factor arising in the system Eqs. (15) and (16), premultiplying the hydrodynamic contribution in the particle force balance and therefore providing a measure of its relative importance compared to the centrifugal term, which is of order 1. For given flow conditions the value of u is known from the solution of the hydrodynamic problem (*12*). It depends on the particle position in the cross-section, but a global order-of-magnitude estimate is obtainable by dividing the maximum value of the stream function by the tube radius (= 1 in dimensionless quantities).

If the ratio of characteristic velocities in Eq. (23) is small, the secondary flows have little effect on the particle, which moves as in a constant centrifugal force field. If the ratio is large, on the other hand, the hydrodynamics dictate the motion of the particle, which remains in suspension. Hydrodynamic results (*12*) indicate that for rotation and axial flow in the same direction, the secondary flow is enhanced significantly as the relative strength of the rotational effects is increased, up to a limiting situation where rotational effects dominate. Simultaneously, the axial flow decelerates with increasing rotation as a result of Coriolis forces. The actual strength of the axial flow is controlled largely by the value of the Dean number, D. Changes in hydrodynamic parameters can thus affect both axial and secondary flows, and represent additional degrees of freedom in design.

These general arguments are confirmed by solutions of Eqs. (11) to (16) for specific situations. Results are presented in dimensional terms for a tube radius of 2 mm. First, the effects of particle size can be seen in Fig. 4, which shows the projections of the trajectories of two particles of different size under constant flow conditions. Both particles are assumed to be at the same position, $(r,\alpha) = (0.1,\pi/2)$, initially. Only the upper half of the cross-section is shown because of symmetry across the center line. For the particular flow conditions chosen to prepare the figure (D = 600, Ta = 10,000), the smaller particle ($\epsilon = 0.00005$) stays in suspension and migrates in the axial direction in a spiraling path, projected in Fig. 4 to a

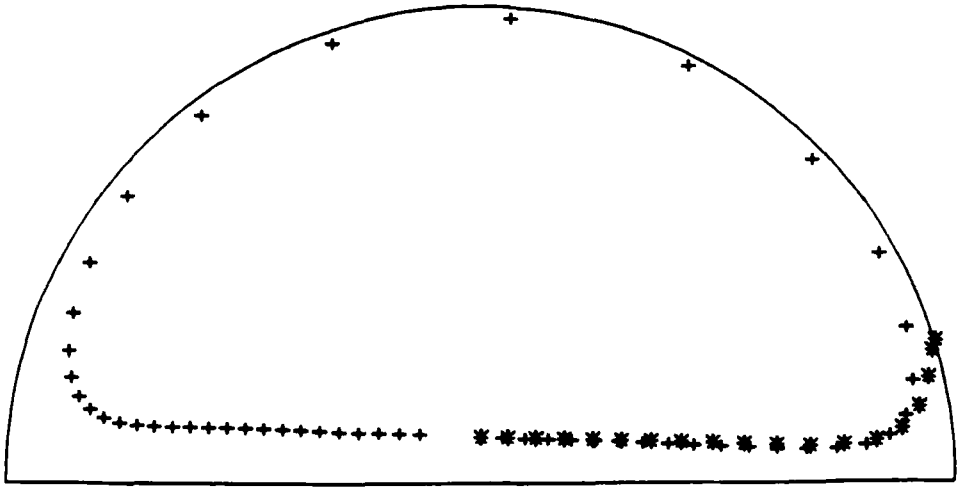

FIG. 4. Effect of particle size on projections of trajectories in cross-sectional plane. Particle characteristics: $\sigma = 2$; (+) $\epsilon = 0.00005$; (*) $\bullet = 0.001$. Flow characteristics: D = 600; Ta = 10,000. Initial conditions: $(r,\alpha) = (0.1,\pi/2)$.

closed path, while the larger one ($\epsilon = 0.001$) sediments. The qualitatively different behavior of the two particles has, as a consequence, a difference in extent of axial migration, as shown in Fig. 5, where axial migration, s', is plotted as a function of time. Because of the qualitatively different suspension behavior, differential axial migration occurs, and this can be amplified through cyclic repetition of the step. The wiggles apparent in the axial migration line of the smaller particle arise during the period the particle spends close to the periphery of the tube, where the axial velocity it experiences is relatively small. Similar effects to those of size arise from differences in particle density.

The differences in behavior seen in Fig. 4 can be predicted by using Eq. (23), where U/U_s takes on values of about 2 and 700 for the large and the small particle, respectively. These values are based on use of the maximum value of the stream function to estimate u, so they are necessarily approximate. However, other situations for which detailed calculations have been performed confirm the utility of Eq. (23) in providing a criterion for predicting whether or not a particle will sediment.

An example of the effects of hydrodynamic parameters is shown in Fig. 6, where the effect of the strength of the axial flow is studied on the

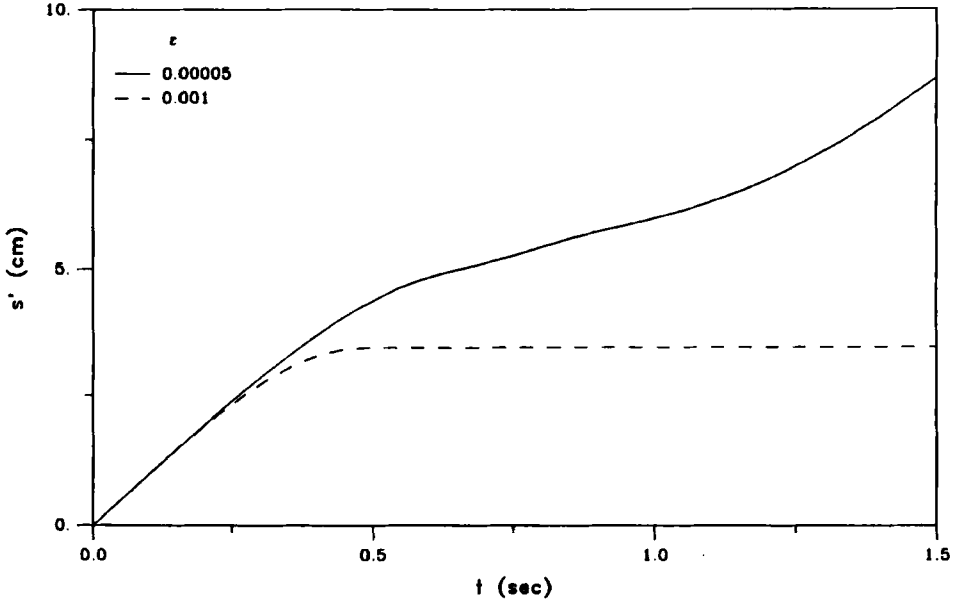

FIG. 5. Effect of particle size on extent of axial migration. Particle characteristics: $\sigma = 2$. Flow characteristics: D = 600; Ta = 10,000. Initial condition: $(r,\alpha) = (0.1,\pi/2)$.

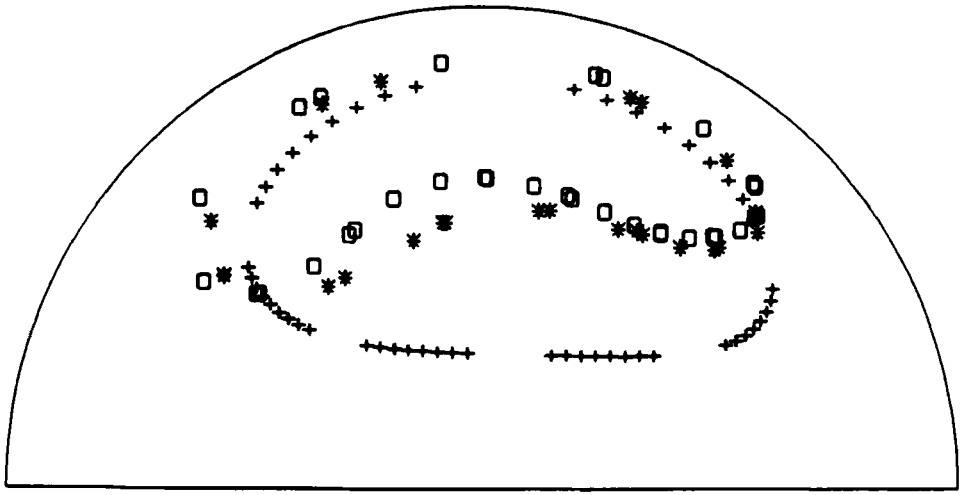

FIG. 6. Effect of hydrodynamics on projections of trajectories in cross-sectional plane. Particle characteristics: $\sigma = 5$; $\epsilon = 0.0005$. Flow characteristics: Ta = 1000; (+) D = 100; (*) D = 2100; (○) D = 5100. Initial condition: $(r,\alpha) = (0.8,\pi/4)$.

trajectory of a particle with $\epsilon = 0.0005$, $\sigma = 5$, and $(r,\alpha) = (0.8,\pi/4)$ as the initial position. The calculations used for preparing the figure allowed enough time for multiple circuits of the particles, and hence the symbols used do not correspond to the sequence of particle positions during one particular cycle. For all the cases shown, the secondary flow is strong enough to keep the particle in suspension, and the trajectories follow the secondary flow streamlines closely. The axial migration as a function of the axial flow strength is shown in Fig. 7. Although all the particles remain in suspension and are thus transported axially, the extent of migration depends on the strength of the primary flow, and Fig. 7 clearly shows the enhancement of axial migration with increasing flow rate. The wiggles seen in the figure for D = 5100 only are due to the fact that, because of the distortion of the streamlines, especially at large values of D, the particle moves close to the wall and hence into a region of small axial velocities. The important parameter in this case is the ratio of the Dean number to the Taylor number, which provides an estimate of the relative strength of axial pumping and rotation.

A very wide range of hydrodynamic conditions is possible, especially when situations where the axial flow and rotation are in opposite directions are included. The resulting range of relative extents of particle motion is consequently also large. It is possible, for example, to use step 2 as a

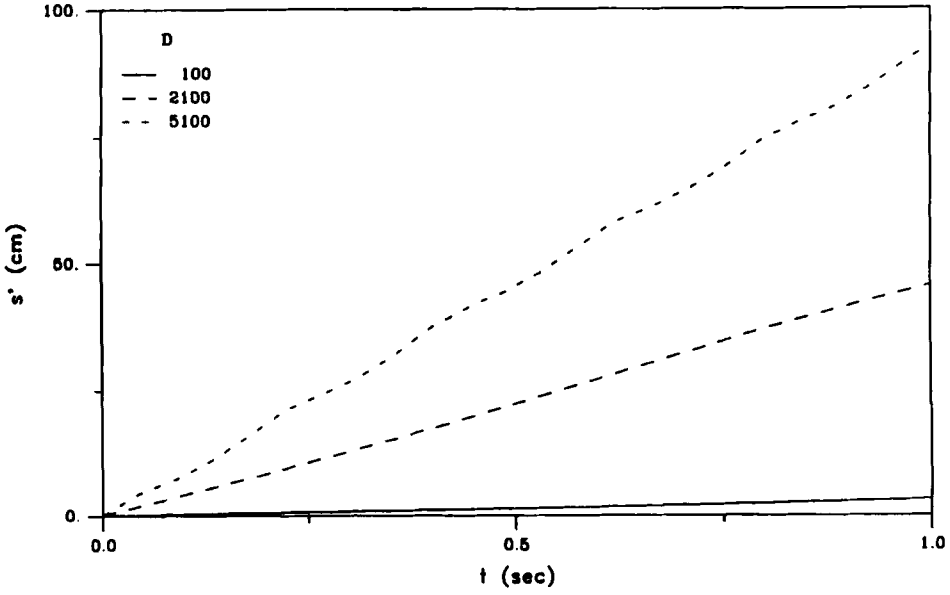

FIG. 7. Effect of hydrodynamics on extent of axial migration. Particle characteristics: σ = 5; ϵ = 0.0005. Flow characteristics: Ta = 1000. Initial condition: $(r,\alpha) = (0.8,\pi/4)$.

preferential sedimentation step instead of a conventional sedimentation step, or for resuspension (step 5) to be performed under laminar flow (*23*).

Since the trajectory of a particle depends on the nature of the flow at its position in the cross-section, the initial position of the particle is important in determining its fate. For fixed hydrodynamic conditions, particles that are close to the periphery of the tube or to the centerline experience relatively weak secondary flows and are more susceptible to sedimentation, while particles in the core of the flow experience stronger secondary flows and can remain in suspension more easily. In order to quantify the influence of different initial conditions on particle migration, simulations were performed for identical particles under fixed flow conditions but with different initial positions. Figure 8 is representative of such simulations in showing the behavior of particles of different size starting at different initial positions in the cross-section. The conditions used in preparing the figure are similar to the experimental conditions (*2*): the hydrodynamic parameters are D = 600, Ta = 1500, and the particles have a relative density σ = 5, with the duration of the cycle being 20 s. The calculations support the earlier qualitative contentions. For the smallest particle size shown, ϵ = 0.0025, all the particles but two in the vicinity of

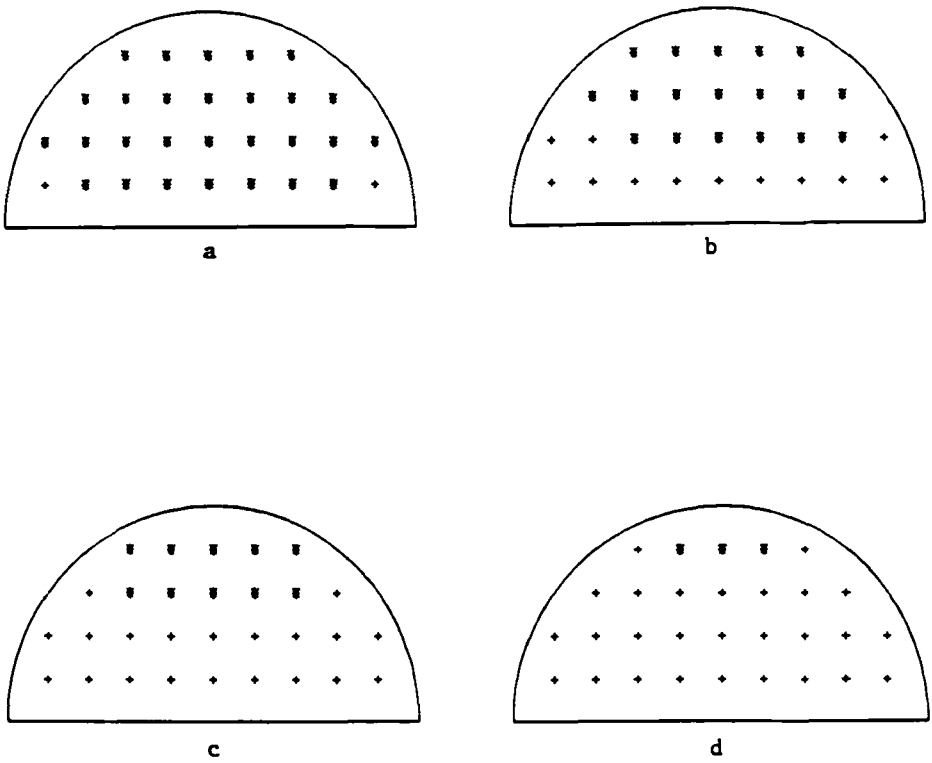

FIG. 8. Particle behavior in cross-sectional plane as a function of initial position. + denotes that a particle sediments and * that it remains in suspension. Particle characteristics: $\sigma = 5$; (a) $\epsilon = 0.0025$; (b) $\epsilon = 0.005$; (c) $\epsilon = 0.0075$; (d) $\epsilon = 0.01$. Flow characteristics: D = 600; Ta = 1500.

the inner and outer walls close to the centerline remain suspended. As the particle size is increased to $\epsilon = 0.005$ and 0.0075, the centrifugal forces become stronger and more particles sediment, while for $\epsilon = 0.01$ the secondary flows are inadequate and practically all particles sediment, with the exception of those starting close to the region of maximum strength of the secondary flow circulation. The tube cross-section can thus be divided into a region close to the walls, with particles starting there sedimenting, and a central core where particles remain in suspension. As particle size is increased, the central core shrinks, and there exists a cut-off value of particle size above which all particles sediment. The shape and size of the central core depend on the flow characteristics, while the duration of the step also affects the outcome. Again, similar conclusions can be drawn from varying particle density instead of particle size.

The effect of the behavior described above on axial migration is shown in Fig. 9 for particles of $\epsilon = 0.005$, with various initial conditions. All particles remain in suspension and hence migrate downstream because of the axial flow, but local differences result in differential migration: particles starting on streamlines close to the wall migrate more slowly because they travel for a significant amount of time near the wall, where axial velocities are small.

Monodisperse Multiparticle Systems

Simulations were performed for systems of particles of different density and size. The values of dimensionless particle density were $\sigma = 5.15$ and 5.75 for the ferric oxide and zirconium oxide particles, respectively, while the range of sizes is discussed later. The hydrodynamic field and the duration of the various steps correspond to the values shown in Table 3.

The results obtained for steps involving axial migration are summarized in Fig. 10, where the extent of axial migration, in centimeters, is plotted against the particle radius, in microns, for the forward (step 2) and the slow backward step (step 4). Based on the experimental particle size distribution data, most of the zirconium oxide particles are sedimented at the

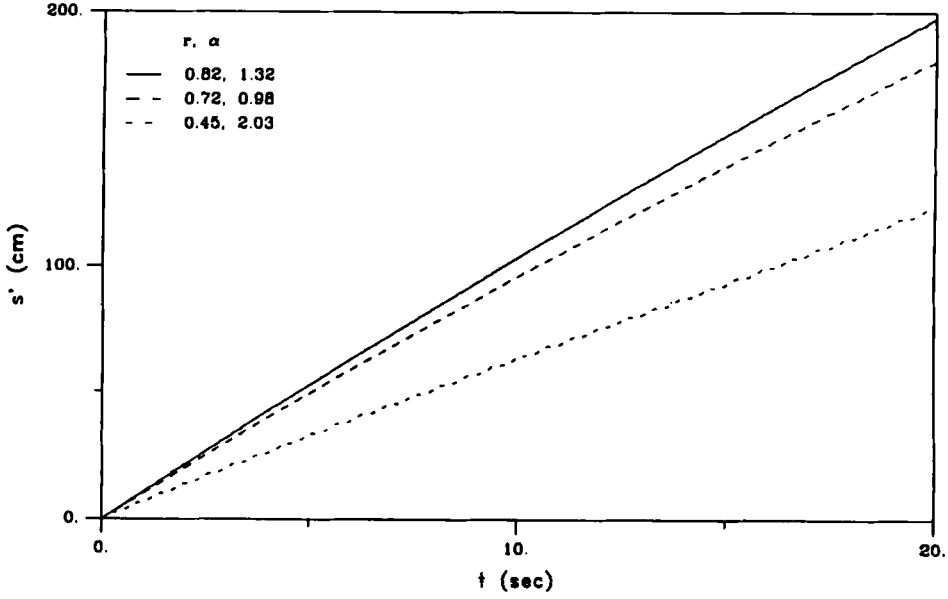

FIG. 9. Effect of initial position on extent of axial migration. Particle characteristics: $\sigma = 5$; $\epsilon = 0.005$. Flow characteristics: D = 600; Ta = 1500.

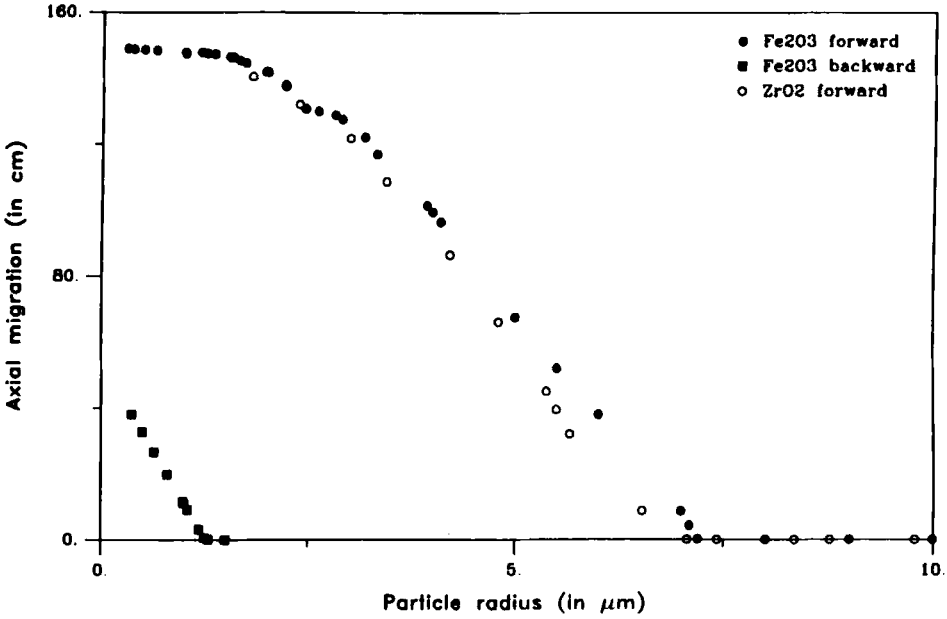

FIG. 10. Average axial migration distance as a function of particle size.

end of step 3, and hence they do not migrate backward during the subsequent slow backward pumping step. This is why only ferric oxide particle results are shown for this step.

Because of the similar densities of the two types of particles, the axial migration distances are almost identical for particles of the same size for the two materials. Hence the experiments (*2*) accomplished classification based primarily on size. Figure 10 indicates that, during the forward pumping step, the secondary flows are strong enough to keep in suspension particles with radii up to approximately 6.7 and 7.2 μm for the zirconium oxide and ferric oxide samples, respectively. A smaller radius does not necessarily imply that all particles are suspended in the fluid because, as explained earlier, this also depends on the initial position of the particles. However, as the particle size is decreased, the fraction of particles remaining in suspension increases. For the most important range of radii between 1 μm and the limit of sedimentation radius for each sample, the following relationships reliably describe the distance traveled (ℓ, in cm) by a particle of radius a_p (in μm) during the forward pumping step:

$$\ell = 164 - 7.33a_p - 2.16a_p^2 \tag{24}$$

for the ferric oxide particles and

$$\ell = 158 - 5.16a_p - 2.82a_p^2 \quad (25)$$

for the zirconium oxide ones. The distance traveled by the ferric oxide particles during the slow backward migration step can be described by the linear relationship

$$\ell = 53.9 - 42.7a_p \quad (26)$$

for particles with a radius in the range 0.2 to 1.25 μm.

Step 3, which plays the role of a complete sedimentation step, is effective for particles with a radius of 1.25 μm or larger. For smaller particles this step is not long enough for complete sedimentation of the entire sample, and this results in migration toward reservoir I during the subsequent slow backward pumping step. This is particularly important for the ferric oxide sample, a significant weight fraction of which is in this size range; this material will migrate as indicated by Fig. 10 and Eq. (26).

The experimental data (*2*) were reported in terms of the concentration ratios for the two particle types in the two reservoirs, plotted as a function of cycle number (N). The concentration ratio, C_N/C_0, is the concentration in the reservoir at the end of cycle N, divided by the initial concentration. The simulation results for the process are presented in the same format, with monodisperse ZrO_2 populations considered here and polydisperse populations in the next subsection.

For the ZrO_2, most of the particles sediment during step 2, so the main motion of the sample is during the fast backward step. Cyclic repetition of the steps results in depletion of reservoir II and a higher concentration of ZrO_2 in reservoir I. A typical run is shown in Fig. 11, where a particle radius of $a_p = 7.5$ μm is used, a value corresponding to the first-order quadrature point. The concentrations in both reservoirs initially change rapidly, until a steady state is reached in which almost all zirconium oxide particles are in reservoir I. The figure also shows the concentration ratio in the coil, calculated by averaging along the coil, i.e., across the various concentration regions separated by fronts, which arise as discussed earlier. The coil is also depleted of particles, and after about 50 cycles the concentration in it falls to zero.

Behavior is completely different for much smaller particles, for instance $a_p = 2.4$ μm as shown in Fig. 12, again for particles with the density of ZrO_2. The differences arise because the secondary flows during the forward pumping step are strong enough to keep the particles in suspension, leading to net motion toward reservoir II. The concentration in reservoir II thus

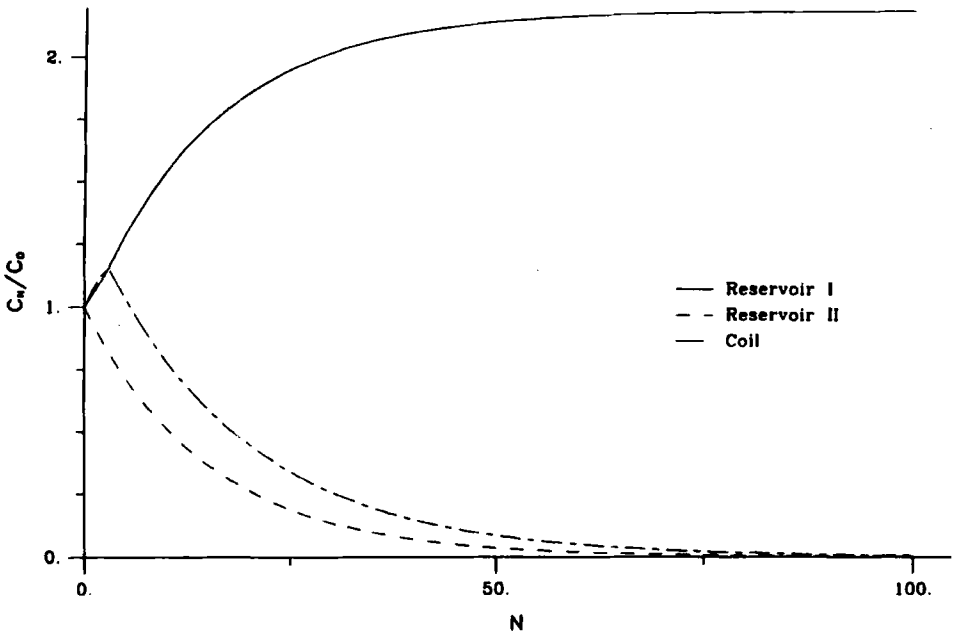

FIG. 11. Concentration ratio as a function of number of cycles. Results for ZrO_2 particles with a_p = 7.5 μm.

increases with the cyclic repetition of the steps, and reservoir I is depleted, while a significant portion of particles is still present in the coil after 100 cycles.

As indicated by the qualitative discussion presented earlier, there is a cut-off particle size a_c between the two sizes considered in Figs. 11 and 12 for which the extents of axial migration during the forward and the backward pumping steps are equal, so that the particles of that size will never leave the coil. This particle size and other characteristics of the particle size distribution determine much of the behavior of the population during the process, and this can be modeled only by taking into account the full distribution; this is done next.

Polydisperse Multiparticle Systems

The particle size distribution data (Table 1) were fitted to the continuous distributions for the zirconium oxide and ferric oxide samples. A comparison is shown for zirconium oxide in Fig. 13, with the experimental data represented as having a constant value in each of the size ranges given.

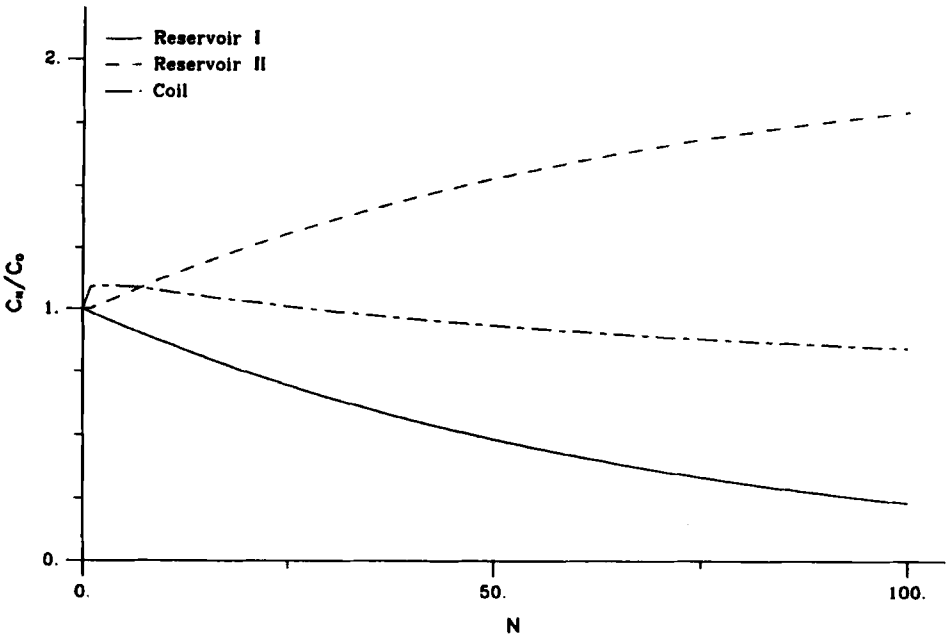

FIG. 12. Concentration ratio as a function of number of cycles. Results for ZrO_2 particles with $a_p = 2.4$ μm.

The beta distribution appears to be closest to the experimental data, and was thus preferred. Both the log-normal and Pearson III distributions satisfy the imposed constraints, but are significantly skewed to smaller particles. Somewhat different fits for these two distributions can be obtained by using different specifications (other than fitting the 50 and 80% fractions).

The ferric oxide sample has a much narrower size distribution and a significantly lower average radius than the zirconium oxide sample. These features make it impossible to find a distribution exactly satisfying the 50 and 80% experimental measurements, but the distributions shown in Fig. 14 are representative of a class depicting the experimental data reasonably. A more extensive evaluation of the sensitivity to the distribution parameters (*23*) indicates that, at least for beta distributions that represent the data reasonably, the quadrature points and the weights are within about 3% of each other despite the relatively wide variation of parameters, suggesting that any of these parameter sets may reasonably be used. There is, however, a more serious problem in describing the two tails of the sample. There is a 5 wt% fraction comprising particles with a radius less

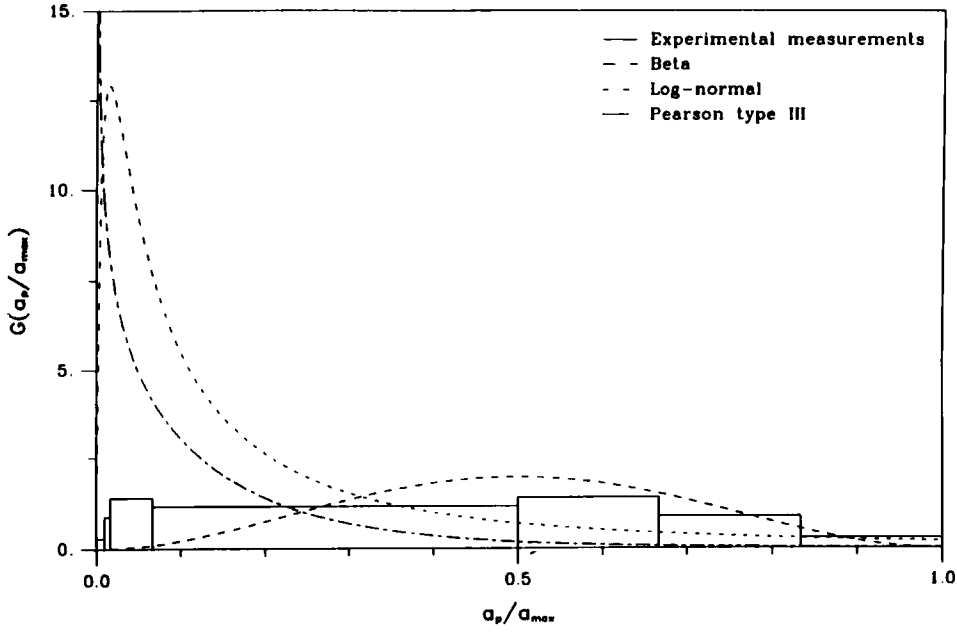

FIG. 13. Particle size distribution for the zirconium oxide sample.

than 0.25 or larger than 5 μm. Since this is a small fraction of the total mass of the system, it would not be expected to play a major role in the subsequent simulations. However, qualitatively different behavior in either or both tails can dramatically change the observed overall behavior of the sample. For example, for the Fe_2O_3 particles, the experimentally observed trend is preferential migration toward reservoir II, but settling of larger particles in the incomplete sedimentation step (step 1) results in net migration of the small particle fraction toward reservoir I, i.e., in the opposite direction.

The beta distribution used to model the zirconium oxide sample results in a cut-off size a_c of 3.75 μm, from which is obtained that 10.3 wt% of ZrO_2 particles show a net migration toward reservoir II, 4.2 wt% migrate so slowly that they remain in the coil after 100 cycles, and the rest (85.5 wt%) migrate toward reservoir I. These long-time results are a function of the distribution only. However, the dynamic behavior leading to this situation requires quadrature over the distribution, as outlined earlier. Calculations for the full distribution were performed for different quadrature orders M until convergence was achieved, as summarized in Fig. 15. The lines showing a concentration ratio larger than 1 (enhancement) correspond to reservoir I, and those with values less than 1 (depletion) to

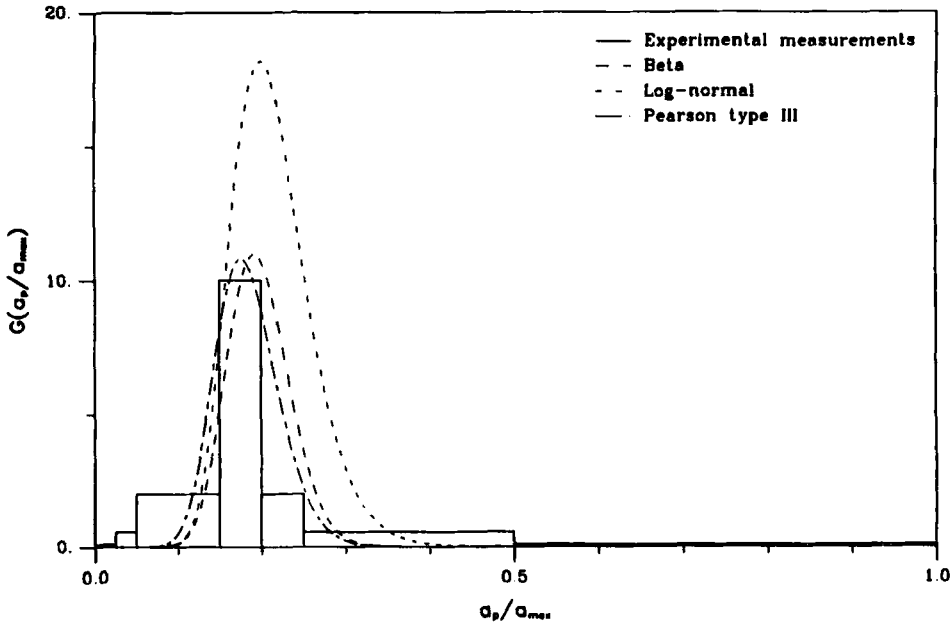

FIG. 14. Particle size distribution for the ferric oxide sample.

reservoir II. The significant differences seen in the model predictions using different orders of quadrature result from the relatively wide size distribution and the qualitatively different behavior in different regions, namely net migration in opposite directions. Since the small-particle tail represents a relatively small fraction of the population, quadrature points are not placed in the tail for small M. It is for this reason that the modified quadrature scheme, discussed earlier, was used to ensure inclusion of representative points in the tail region.

The calculations with the modified quadrature are shown in Fig. 16, with a quadrature order M here implying the use of $M + 2$ terms: M as before and 2 additional ones accounting for the correct weight fraction ratio of the different population regions. The relative error between the two most refined calculations at the end of the last cycle ($N = 100$) is around 1.7%. The most refined calculations indicate that steady state is approached after roughly 50 cycles, with 86% of the zirconium oxide in reservoir I. The dynamic behavior is more sensitive than the steady state to the selection of the quadrature points, and the sensitivity of the steady state is essentially eliminated by the modified quadrature scheme.

Because of the relatively narrow size distribution of the ferric oxide

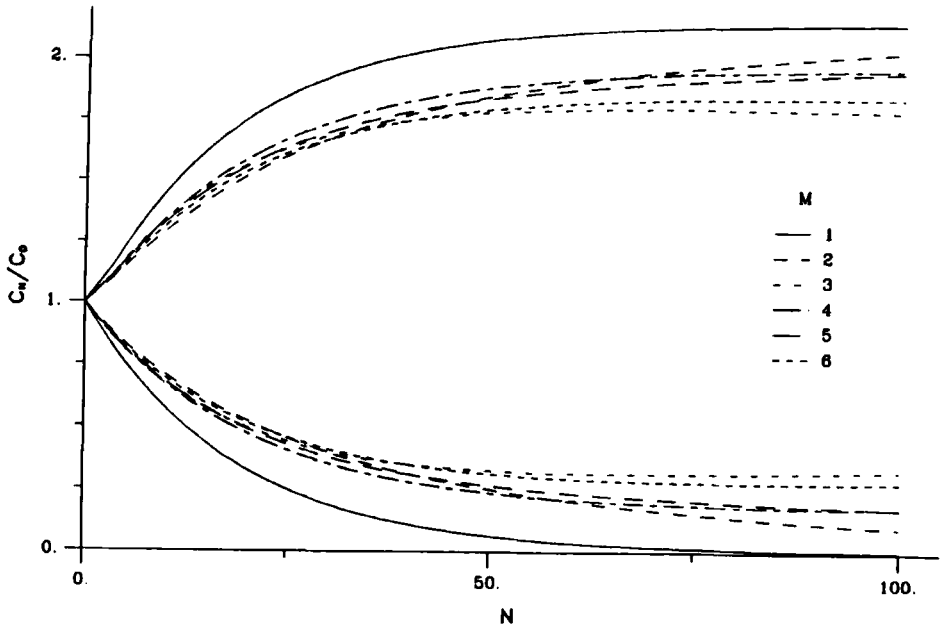

FIG. 15. Concentration ratio as a function of number of cycles. Convergence behavior for ZrO_2 for different quadrature orders.

sample, its steady-state behavior is more clear-cut than that of the zirconium oxide. For instance, using a beta distribution with parameters a = 21.191 and b = 92.136, 98.98 wt% of the population is transported toward reservoir II, with no accumulation inside the spinning coil. In this case a low-order quadrature is adequate for convergent results, as shown in Fig. 17. The enhancement line here corresponds to the concentration in reservoir II and the depletion one to that in I. Comparison of this figure with the corresponding one for zirconium oxide (Fig. 16) verifies that fractionation is accomplished.

Because, as mentioned earlier, a distribution identically satisfying the experimental measurements of weight fraction over the specific particle size range could not be found for the ferric oxide sample, several distributions satisfying the 50 and 80% weight fraction conditions as closely as possible were tried, with very similar results to those shown in Fig. 17. In addition, in view of the effects of tails on overall behavior, an alternative distribution, now satisfying the 80 and 95% weight fraction conditions, was also tried; this distribution should be compared to that used in Fig. 14, which places 99.98% of the mass in the radius range from 0.25 to 5 μm,

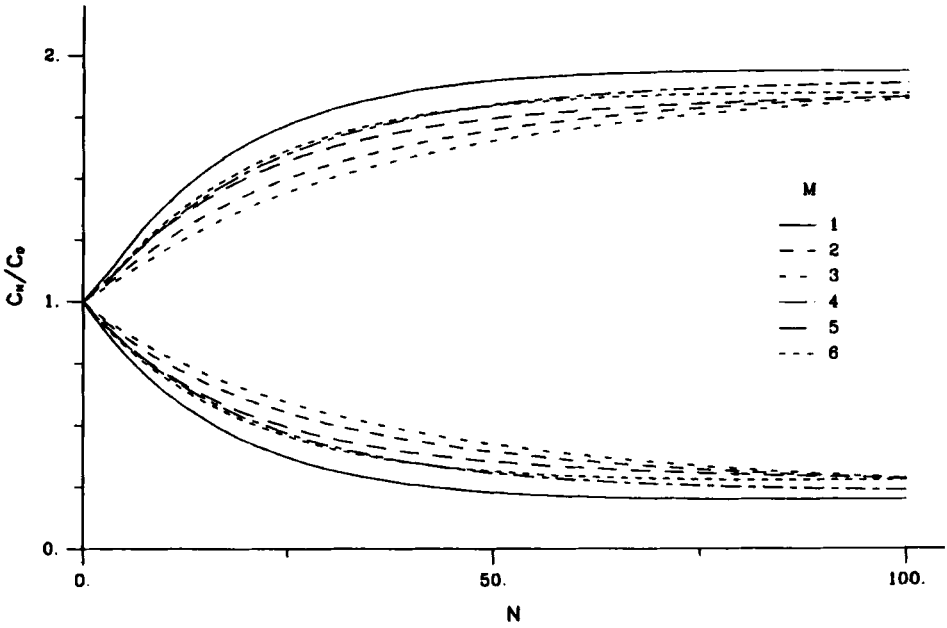

FIG. 16. Concentration ratio as a function of number of cycles. Convergence behavior for ZrO_2 for different quadrature orders using modified quadrature procedure.

compared to the experimentally reported value of 95%. The additional distribution, a beta distribution with parameters $a = 2.872$ and $b = 26.128$, is skewed toward lower particle sizes compared to the original one, but it, too, predicts that more than 99.9% of the sample migrates toward reservoir II. However, a major difference is that the new distribution suggests that 58% of the sample comprises particles small enough for sedimentation to be incomplete during step 3, while the corresponding number for the original one was 0.3%, and this affects the dynamic behavior. Figure 18 shows that accounting for the smaller particle sizes reduces the calculated efficiency of the separation, as characterized by the dynamics of attaining the long-time fractionation situation. These results emphasize the importance of a detailed knowledge of the particle size distribution.

The theoretical predictions for a system consisting of a mixture of ferric and zirconium oxide particles are shown in Fig. 19, together with the experimental data (*2*). The predictions shown for the ferric oxide sample are those using the distribution function that accounts for the tail at small particle sizes. The model reproduces the qualitative experimental trends: the zirconium oxide particles are transported toward reservoir I, and the

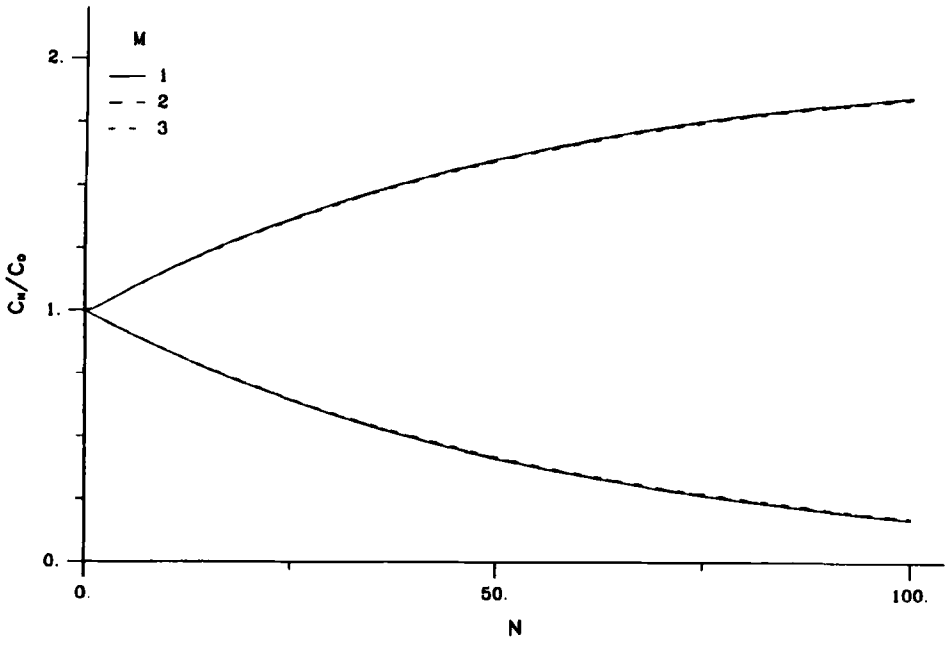

FIG. 17. Concentration ratio as a function of number of cycles. Convergence behavior for Fe_2O_3 for different quadrature orders.

ferric oxide toward II, with transport of ZrO_2 faster than that of Fe_2O_3. Zirconium oxide particle transport is essentially complete after 50 cycles, while ferric oxide transport is incomplete after even 100 cycles. Additional calculations for ferric oxide predict an approach to steady state at around 200 cycles.

Since a steady state was reached experimentally only for the zirconium oxide particles, it is only for this sample that an evaluation of the theory is possible for the prediction of the cut-off size a_c. Agreement is good for the depletion prediction (reservoir II), but efficiency is somewhat overpredicted for the final concentration in reservoir I. The agreement is encouraging in view of the inclusion of no adjustable parameters at all in the calculations.

The discrepancies in predictions of both steady-state and dynamic behavior may result at least in part from the presence of dead volume in the experimental apparatus, in the form of connecting lines and the rotating seal assembly. Together these account for an additional volume equal to 39% of the coil volume. The presence of the connecting lines is expected to affect the separation adversely, as was verified experimentally (*32*). To

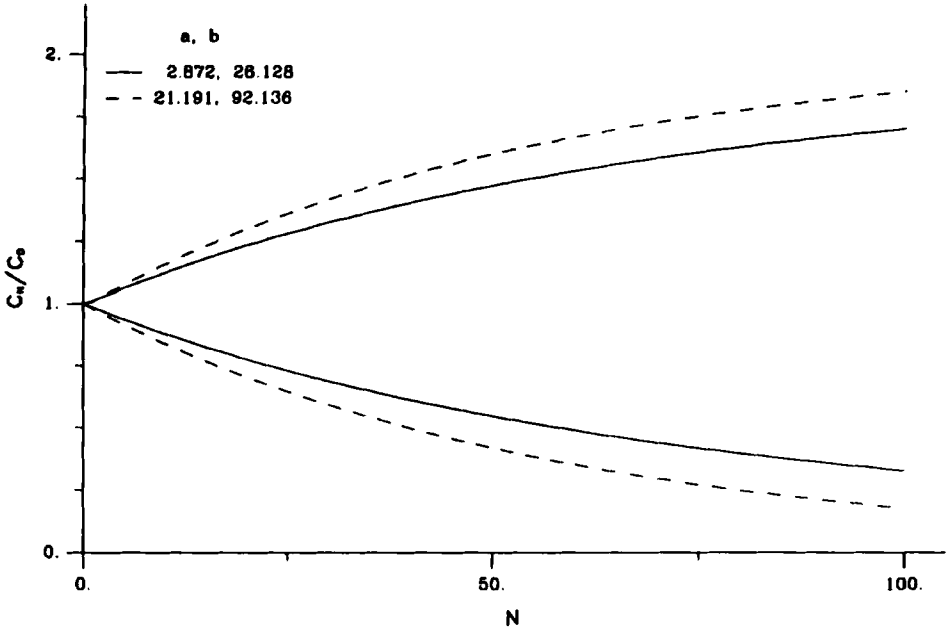

FIG. 18. Concentration ratio as a function of number of cycles. Effect of distribution parameters for Fe_2O_3.

account for the dead volume, the model was modified by the addition of a compartment at each end of the coil, with plug flow assumed in each. The volume of each additional compartment was taken as 10.5 mL, corresponding to the measured 6 mL of connecting line at each end of the coil and 9 mL overall volume of the spinning seal assembly. Thus the modification of the model did not introduce any adjustable parameters.

The incorporation of dead volumes in the model was found to increase the mass of particles predicted to accumulate in the coil. Accumulation of particles in the coil is not a consequence only of the existence of dead volumes and it cannot be avoided completely, but the presence of dead volumes can significantly increase the extent of accumulation in the coil and consequently drastically reduce the efficiency of the separation. This occurs because the dead volumes increase the effective coil length, with the effective migration velocity unaffected. This slows the fractionation dynamics, but in addition the size-neutral plug flow migration in the dead volume increases the size range Δa around a_c (Fig. 2) for which particles will never leave the coil. Hence both reservoirs are depleted in their steady-state concentrations, in addition to the effect on dynamic behavior.

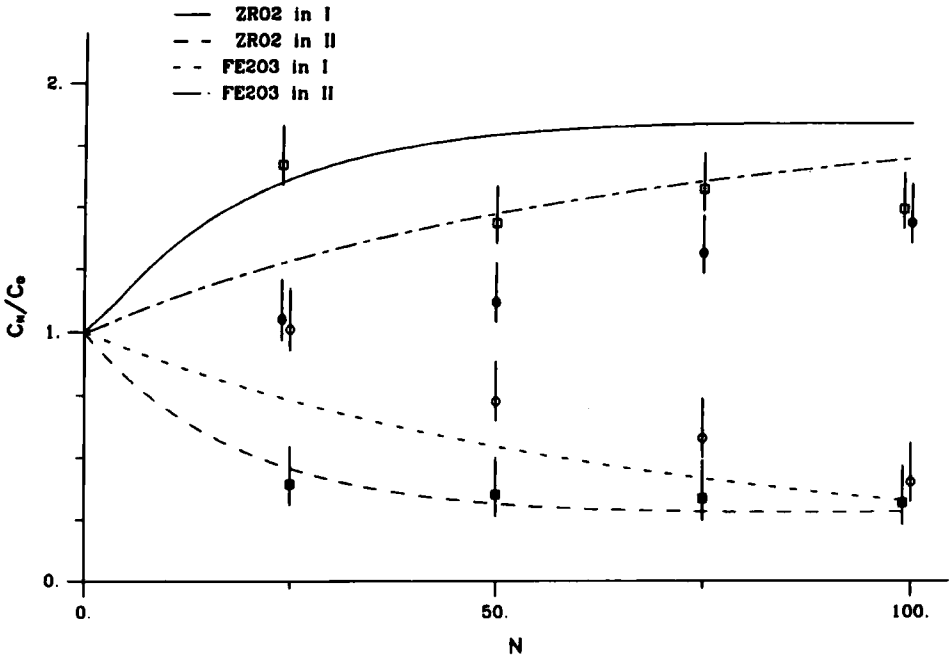

FIG. 19. Comparison of theoretical predictions with experimental data. (□) ZrO_2; (○) Fe_2O_3. Open symbols: reservoir I; filled symbols: reservoir II. Vertical bars: estimated experimental uncertainty (*2*).

The simulation of the experimental results was modified to include the connecting tubing, with results of the most accurate calculations performed shown in Fig. 20, together with the experimental results for comparison. The addition of dead volumes in the system does not alter the physical behavior, and all the qualitative trends of Fig. 19 are reproduced here. However, the tubing causes a lag for the first few cycles before the concentration of the reservoir that will eventually be enriched starts to increase for both samples. This lag period depends on the actual volume of the connecting lines and is increased as the dead volumes increase relative to the volume of the pumping stroke.

The extent to which a particle sample is affected by dead volumes depends on the relative positions of the mean of the distribution and the cut-off size around which the region consisting of particles accumulating in the coil is centered. Because of this, the zirconium oxide sample is affected more than the ferric oxide sample, and the agreement of the simulations with long-time behavior seen experimentally is improved. The amount of

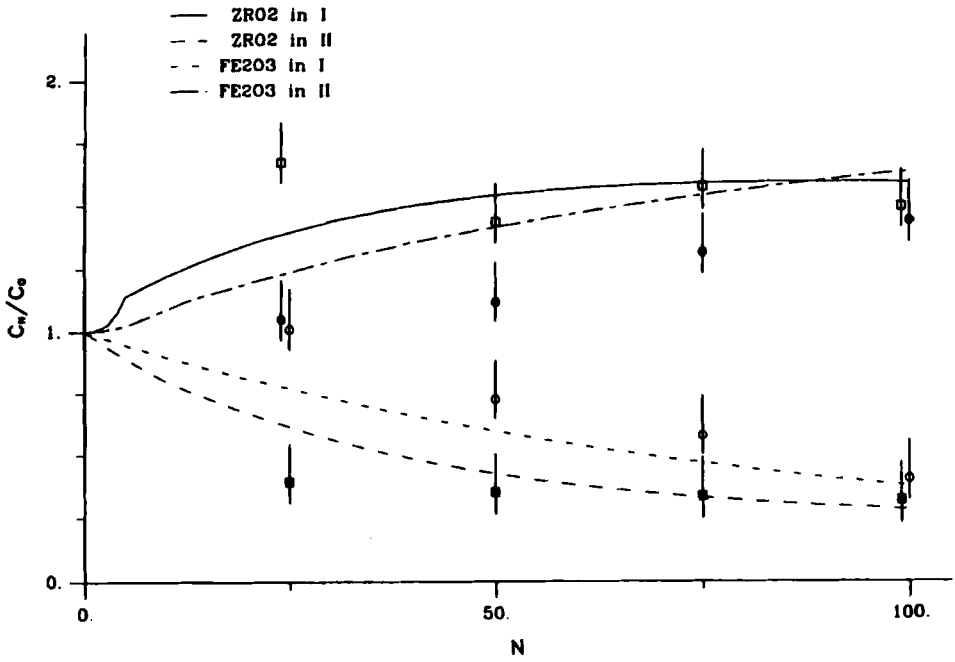

FIG. 20. Comparison of theoretical predictions with experimental data, with inclusion of 10.5 mL of dead volume at each end of coil. Notation as for Fig. 19.

each component transferred to the desired reservoir after 100 cycles was found to be around 85 and 81% for the zirconium and ferric oxide particles, respectively, compared with the experimentally reported value of nearly 80%.

The approach to steady state predicted for the zirconium oxide population (cf. Figs. 19 and 20) is delayed because of the reduction of the separation efficiency of each individual cycle. However, the results for the ferric oxide sample appear to deviate most from the experimental data. In the experiments, a pronounced lag in the change of ferric oxide concentrations in both reservoirs is observed, an effect that is not observed in the simulations. This discrepancy may be related to the uncertainties associated with the use of the continuous distribution in the simulations. In particular, as noted earlier, the existence of tails in the distribution showing different features from its central portion can considerably change the overall observed behavior of the sample. For the distribution used to describe the ferric oxide sample, the simulations find that 57% of the particle mass undergoes backwash during the slow backward pumping step, and hence

a significant portion of the sample is moved away from the concentrated reservoir during one step of the cycle. The overall behavior of the ferric oxide sample is affected strongly by this portion, and using a different distribution can result in significantly different predictions, although the general trends and qualitative behavior are not altered. This observation emphasizes the need for an accurate representation of the particle size distribution, which unfortunately is not possible based on the available experimental data.

CONCLUSIONS

The theoretical predictions obtained for the experimental conditions of Lennartz et al. (*2*) capture all the qualitative trends reported in the experiments. In addition, the quantitative agreement between theory and experiment is reasonable. The most important factor missing for reliable modeling appears to be the detailed and accurate knowledge of the particle size distributions. The distributions used appear successful in predicting quite accurately the enrichment-to-dilution ratios measured experimentally, a consequence of the fraction of the mass of the sample below the cut-off size, but the reliable prediction of the dynamic behavior is more delicate and requires more detailed information about the full particle size distribution.

Various assumptions incorporated in the model are also expected to affect the predictions. Classification can be affected by the flow transients, particle–particle interactions, inertial effects, and axial dispersion effects that have been neglected. However, the effects included in the formulation presented here account for the most important features of observed behavior, and order-of-magnitude estimates of the relative contributions of these effects allow the consequences of parameter changes to be considered approximately without the detailed computations presented here; such calculations are shown by Daskopoulos (*23*).

Acknowledgment

The support of the National Science Foundation, under Grant CBT-8746050, is gratefully acknowledged.

REFERENCES

1. J. C. Giddings, K. D. Caldwell, and H. K. Jones, in Particle Size Distribution: Assessment and Characterization (T. Glidden, ed.), (ACS Symp. Ser. 332), American Chemical Society, Washington, D.C., 1987, pp. 215–230.
2. J. W. Lennartz, M. B. Gorensek, and R. J. Adler, *AIChE J., 33,* 506 (1987).
3. R. J. Adler, M. B. Gorensek, M. E. Landin, M. M. Menon, J. S. Papanu, and H. F. Trost, Paper Presented at ACS National Meeting, New York, 1981.

4. R. J. Adler, M. B. Gorensek, M. M. Menon, and J. S. Papanu, Paper Presented at AIChE Annual Meeting, Los Angeles, 1982.
5. J. S. Papanu, R. J. Adler, M. B. Gorensek, and M. M. Menon, *AIChE J., 32,* 798 (1986).
6. P. T. Palepu, R. J. Adler, and C. K. Wu, Paper Presented at AIChE Annual Meeting, New York, 1987.
7. R. C. Wilhelm, A. W. Rice, and A. R. Bendelius, *Ind. Eng. Chem., Fundam., 5,* 141 (1966).
8. R. C. Wilhelm, A. W. Rice, R. W. Rolke, and N. H. Sweed, *Ibid., 7,* 337 (1968).
9. J. C. Giddings, *Sep. Sci., 1,* 123 (1966).
10. J. C. Giddings, *Chem. Eng. News, 66*(41), 34 (1988).
11. J. C. Giddings, F. Yang, and M. N. Myers, *Anal. Chem., 46,* 1917 (1974).
12. P. Daskopoulos and A. M. Lenhoff, *J. Fluid Mech., 217,* 575 (1990).
13. J. Happel and H. Brenner, *Low Reynolds Number Hydrodynamics,* 2nd rev. ed., Nijhoff, Dordrecht, 1973.
14. H. Brenner, *Adv. Chem. Eng., 6,* 287 (1966).
15. L. G. Leal, *Annu. Rev. Fluid Mech., 12,* 435 (1980).
16. J. F. Brady and G. Bossis, *Ibid., 20,* 111 (1988).
17. R. G. Cox, *Int. J. Multiphase Flow, 1,* 343 (1974).
18. S. I. Rubinow and J. B. Keller, *J. Fluid Mech., 11,* 447 (1961).
19. P. G. Saffman, *Ibid., 22,* 385 (1965).
20. B. P. Ho and L. G. Leal, *Ibid., 65,* 365 (1974).
21. P. Vasseur and R. G. Cox, *Ibid., 78,* 385 (1976).
22. R. G. Cox and S. K. Hsu, *Int. J. Multiphase Flow, 3,* 201 (1977).
23. P. Daskopoulos, "Flow in Separations Processes in Rotating Helically Coiled Tubes," PhD Thesis, University of Delaware, 1989.
24. A. Falade and H. Brenner, *J. Fluid Mech., 154,* 145 (1985).
25. F. A. Zenz and D. F. Othmer, *Fluidization and Fluid–Particle Systems,* Reinhold, New York, 1960.
26. M. M. Denn, *Process Fluid Mechanics,* Prentice–Hall, Englewood Cliffs, New Jersey, 1980, Chap. 16.
27. J. S. Halow and G. B. Wills, *AIChE J., 16,* 281 (1970).
28. R. Aris, *Ibid., 35,* 539 (1989).
29. P. J. Davis and P. Rabinowitz, *Methods of Numerical Integration,* 2nd ed., Academic, Orlando, Florida, 1984.
30. S. K. Shibata, S. I. Sandler, and R. A. Behrens, *Chem. Eng. Sci., 42,* 1977 (1987).
31. J. K. Patel, C. H. Kapadia, and D. B. Owen, *Handbook of Statistical Distributions,* Dekker, New York, 1976.
32. J. W. Lennartz, Personal Communication, 1989.

Received by editor March 23, 1990